Deep-tissue anatomical imaging of mice using carbon nanotube fluorophores in the second near-infrared window

Kevin Welsher[1], Sarah P. Sherlock[1], and Hongjie Dai[2]

Department of Chemistry, Stanford University, 333 Campus Drive #121, Stanford, CA 94305

Edited by Charles Lieber, Harvard University, Cambridge, MA, and approved April 15, 2011 (received for review October 6, 2010)

Fluorescent imaging in the second near-infrared window (NIR II, 1–1.4 μm) holds much promise due to minimal autofluorescence and tissue scattering. Here, using well-functionalized biocompatible single-walled carbon nanotubes (SWNTs) as NIR II fluorescent imaging agents, we performed high-frame-rate video imaging of mice during intravenous injection of SWNTs and investigated the path of SWNTs through the mouse anatomy. We observed in real-time SWNT circulation through the lungs and kidneys several seconds postinjection, and spleen and liver at slightly later time points. Dynamic contrast-enhanced imaging through principal component analysis (PCA) was performed and found to greatly increase the anatomical resolution of organs as a function of time postinjection. Importantly, PCA was able to discriminate organs such as the pancreas, which could not be resolved from real-time raw images. Tissue phantom studies were performed to compare imaging in the NIR II region to the traditional NIR I biological transparency window (700–900 nm). Examination of the feature sizes of a common NIR I dye (indocyanine green) showed a more rapid loss of feature contrast and integrity with increasing feature depth as compared to SWNTs in the NIR II region. The effects of increased scattering in the NIR I versus NIR II region were confirmed by Monte Carlo simulation. In vivo fluorescence imaging in the NIR II region combined with PCA analysis may represent a powerful approach to high-resolution optical imaging through deep tissues, useful for a wide range of applications from biomedical research to disease diagnostics.

near-infrared imaging | photoluminescence | principal component analysis imaging | dynamic contrast imaging | deep-tissue imaging

Fluorescence is an important imaging modality in life sciences and medicine (1) because of its ability to resolve features down to the diffraction limit and beyond (2, 3). The benefit of higher resolution unfortunately comes at the cost of limited tissue penetration depth (4). Absorption by biological tissue and water is one factor that leads to attenuation of signal proportional to the depth of the feature of interest. To overcome this problem, much research has focused on developing and implementing fluorescent probes in the "biological transparency window" near 800 nm (here, NIR I) (5). This NIR I transparency window is defined by a local minimum in the absorption spectrum of biological tissue, bounded by hemoglobin and water absorption (Fig. 1*C*) at shorter and longer wavelengths, respectively. Many commercially available probes lie within this region, including commonly used cyanine dyes such as indocyanine green (ICG) and Cy 5.5 (6), as well as semiconductor quantum dots (QDs) (7).

Although the traditional NIR probes outperform probes that emit at shorter wavelengths in the visible region, the definition of biological transparency window by absorption only leads to an incomplete assessment of the behavior of photons in turbid media. This is because photons emitted from a source embedded in turbid media, such as tissue, can be attenuated by both absorption and scattering events. Depth penetration in tissue is defined as $\delta = (3\mu_a(\mu_a + \mu_s'))^{-1/2}$, where μ_a is the absorption extinction coefficient, $\mu_s'(\sim\lambda^{-w})$ is the reduced scattering coefficient, and δ is the resulting penetration depth. The exponent, w, depends on the size and concentration of scatterers in the tissue and ranges from 0.22 to 1.68 for different tissue (Fig. 1*D*) (8). Because of the relatively short wavelength of electromagnetic radiation emitted from traditional fluorophores (450–850 nm), coupled with the inverse wavelength of dependence of both Mie and Rayleigh scattering, the penetration depth can be greatly affected by the scattering nature of the tissue in question (Fig. 1*D*). The effect of scattering on the effective penetration depth of tissue has been observed experimentally (8, 9) and modeled via simulation (10), with the consensus result being that the penetration depth can be maximized at wavelengths between 1 and 1.4 μm, called the second near-infrared window (NIR II).

Currently, there is a dearth of available fluorophores emitting in this beneficial region. QDs (11) such as PbSe (12), PbS (13), and CdHgTe (14) are promising candidates for imaging in the NIR II; however, in vivo animal imaging in the NIR II region with QDs has not been carried out thus far. As an alternative, single-walled carbon nanotubes (SWNTs) have shown promise as fluorescent imaging agents in the NIR II both in vitro and in vivo (15–18). In this work, we apply bright, biocompatible SWNTs as NIR II fluorophores for video-rate in vivo imaging. Video-rate fluorescent imaging of intravenously injected SWNTs allows crisp resolution of anatomical features via the application of dynamic contrast imaging through principal component analysis (PCA), as first developed by Hillman and Moore using NIR I–based fluorophores (19). Both the raw video and time-based dynamic contrast-enhanced images are used to investigate the pathway of SWNTs through the mouse anatomy up to 130 s postinjection (p.i.). Finally, we perform imaging on mock tissue phantoms to determine the effect of using an NIR II– versus an NIR I–emitting fluorophore. These experimental results are backed up by Monte Carlo simulations, showing the beneficial effects of reduced tissue scattering on deeply embedded fluorophores emitting at longer wavelengths in the NIR II region.

Results and Discussions

Video-Rate NIR II Fluorescence Imaging of Mice. Video-rate imaging (see Movies S1 and S2) revealed that the path through the body for water-soluble SWNTs (length approximately 200–500 nm; see Fig. S1 for an atomic force microscopy image) (18) coated by PEGylated phospholipid (DSPE-mPEG) (20), as monitored by their inherent NIR fluorescence, is similar to what is expected for tail-vein injection (21). Following injection, the oxygen-poor

Author contributions: K.W., S.P.S., and H.D. designed research; K.W. and S.P.S. performed research; K.W. and S.P.S. analyzed data; and K.W., S.P.S., and H.D. wrote the paper.

The authors declare no conflict of interest.

This article is a PNAS Direct Submission.

[1]K.W. and S.P.S. contributed equally to this work.

[2]To whom correspondence should be addressed. E-mail: hdai1@stanford.edu.

This article contains supporting information online at www.pnas.org/lookup/suppl/doi:10.1073/pnas.1014501108/-/DCSupplemental.

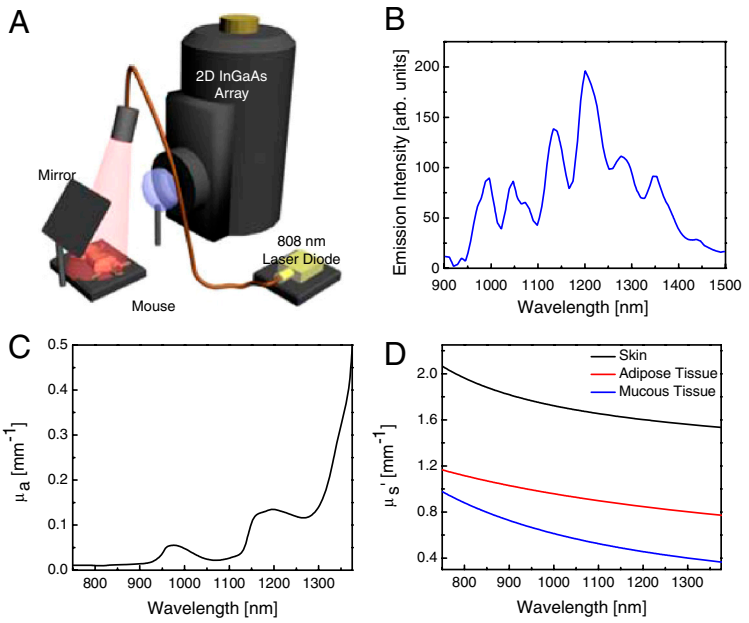

Fig. 1. NIR II imaging. (*A*) Schematic of NIR II imaging setup. Anaesthetized mice are illuminated from above with 808-nm light. NIR fluorescence (1,100–1,700 nm) is filtered and imaged onto a 2D InGaAs array. (*B*) Fluorescence spectrum of biocompatible DSPE-mPEG functionalized SWNTs excited at 808 nm, showing several emission peaks spanning the NIR II region. (*C*) Absorption coefficient, μ_a, of water, showing the increased absorption of water in the NIR II compared to the NIR I. (*D*) Reduced scattering coefficient, μ_s', for skin, adipose tissue and mucous tissue as derived in ref. 8, all showing decreased scattering with increasing wavelength.

blood travels to the heart and lungs to be oxygenated before being distributed throughout the body. This is evidenced by the high contrast of the lung features in the mice in both back and side views (3.5 s p.i.; Fig. 2 *A* and *E*). Following this spike in intensity, the lung contrast fades, indicating the spread of the nanotube-rich oxygenated blood to the rest of the circulatory system. Concurrent to the loss of lung contrast is a peak in kidney contrast, as shown in the images at 5.2 s p.i. (Fig. 2 *B* and *F*) and region of interest (ROI) time courses (Fig. 2 *I* and *J*; see Fig. S2 for ROI locations and raw ROI time-course measurements with animal breathing). The increased signal at these early time points is a result of the nanotube-rich blood passing through the highly vascularized kidneys. Following the peak in kidney contrast, the kidney levels decrease toward its mean signal (Fig. 2 *I* and *J*). The one-pass circulation time of blood in a mouse was previously determined to be approximately 15 s (22). This time frame aligns with the appearance of a steady-state signal seen in ROI measurements in Fig. 2. During the first 15 s of imaging, the SWNT-rich blood is distributed throughout the body. After the first pass of SWNT-rich blood, the liver, lungs, muscle, and kidneys all show fairly constant signal indicating consistent blood flow in these organs.

It should be noted that the strong signal does not necessarily indicate SWNT accumulation and retention in organs, but could be due to blood perfusion and microcirculation within organs, or temporary SWNT extravasation prior to being rereleased into the

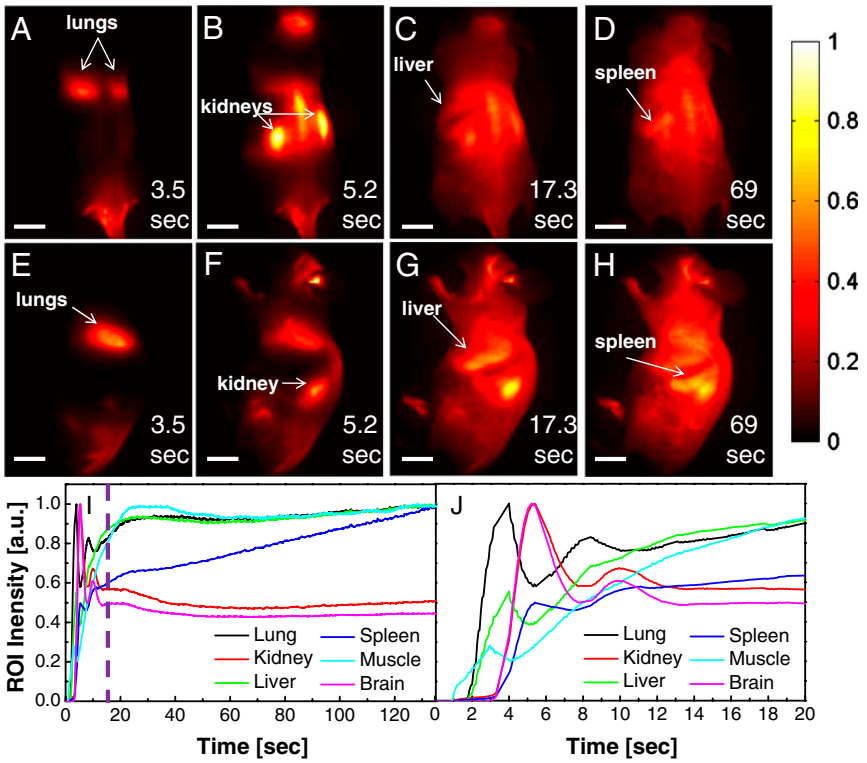

Fig. 2. Video-rate imaging of SWNTs in a live mouse. Frames from video imaging of mice injected with SWNTs. At (*A* and *E*) 3.5 s following tail-vein injection, the lungs are the dominant feature, corresponding to flow of the oxygen-poor, SWNT-rich blood to the lungs. (*B* and *F*) At 5.2 s, the SWNT-rich blood flows through the highly vascularized kidney. (*C* and *G*) The liver becomes apparent at 17.3 s p.i., whereas the (*D* and *H*) spleen becomes visible at 69 s p.i.. Scale bars in all images represent 1 cm. (*I* and *J*) Normalized ROI time courses over the organs in the raw images. For clarity, frames where the mouse is breathing were not included. The lungs, kidney, and liver show large spikes shortly after injection (approximately 5 s) followed by a return to a steady-state intensity within 20 s. The purple line in *I* shows the predicted time for blood to make one pass through the body, leading to a steady-state SWNT signal in the body. The spleen shows a deviation from this behavior, showing no early spike and a monotonic increase in signal with increasing time.

circulating blood. It is unlikely that the signal is solely due to SWNT accumulation and retention because the time frame of the video-rate imaging (approximately 2 min) is much shorter than the circulation half-life of DSPE-mPEG functionalized SWNTs (approximately 5 h) (20). The strong kidney signal observed during imaging up to approximately 2 min p.i. does not support SWNT accumulation and retention because previous work has shown once nanotubes are no longer circulating, the level of SWNT accumulation in the kidneys is only approximately 1% of the injected dose per gram (approximately 1% ID/g) of tissue (20). As a result, the peak in kidney signal is likely to be mainly due to SWNTs circulating in the blood stream shortly after injection. The SWNT signal in the head region in Fig. 2*B* is likely due to SWNT circulation rather than accumulation in the brain because little evidence exists that DSPE-mPEG functionalized SWNTs cross the blood–brain barrier (20).

The behavior of organs in the reticuloendothelial system (RES), mainly the liver and spleen, are of particular interest in this study. It has been shown that clearance of SWNTs functionalized by DSPE-mPEG is through the RES system, with the liver and spleen showing uptake of approximately 35% and approximately 25% ID/g, respectively, at 1 d p.i. (20) The spleen is easily identified in the raw images at approximately 69 s p.i. (Fig. 2 *D* and *H*). The spleen ROI shows continuously increasing signal over the course of the video imaging with no peak shown immediately following injection, contrary to what was seen from the lung and kidney ROIs (Fig. 2 *I* and *J*). Although the physical meaning of this has not been fully investigated, the continual increase in fluorescence intensity could be attributed to SWNT extravasation or increasing microcirculation throughout the spleen. Previous studies have shown that the splenic marginal zone fills prior to the splenic red pulp (23). Initial signal in the spleen could be due to filling of the marginal zone, followed by an increase in signal as SWNT-rich blood accumulates in the adjacent red pulp region.

The liver can be resolved in the raw images starting at approximately 17 s p.i. (Fig. 2 *C* and *G*). The liver ROI shows similar behavior to both the lungs and kidney and does not follow the same behavior as the spleen despite the high SWNT accumulation at longer times as previously observed by ex vivo biodistribution studies (Fig. 2 *I* and *J*) (20). It is likely that the liver has not begun to accumulate a significant amount of SWNTs at such early time points, and the signal seen is merely a reflection of the circulation of SWNT-rich blood through the organ.

Anatomical Resolution Through PCA. In an effort to gain further anatomical resolution, PCA was applied to the time series of images based on the intrinsic fluorescence of SWNTs in NIR II. PCA is a common statistical processing method for compressing high-dimensional data into a lower-dimensional form by choosing only the highest variance components of the dataset (24). PCA is performed on groups of images by considering each pixel to be an observation that varies over the variable time. More information about PCA is provided in the *SI Text* and Fig. S3.

Dynamic contrast imaging was applied to observe behavior of organs that are not easily seen or resolved from nearby features in the raw images. As shown by Hillman and Moore (19), dynamic contrast imaging via PCA can be a powerful tool to achieve anatomical resolution of major organs. During initial circulation of a fluorophore, organ signal has the highest variation over time. Furthermore, different organs vary differently in time because of differences in blood volume flow rates for various organs (25), allowing them to be distinguished when proper statistical treatment is applied.

PCA of a time series of images was used as a tool to group pixels that vary similarly in time. As pixel variation within a single organ will be similar, PCA is able to group pixels belonging to the same organ. By defining axes in N-dimensional space that correlate to the highest variance and are mutually orthogonal, we translated the correlated time behavior of the pixels into spatial (in this case anatomical) resolution. Upon performing PCA analysis on the first 130 s p.i., we clearly observed four major organs of interest (Fig. 3) because of their high, but distinct, variance in time. In addition, we believe we were able to resolve an additional organ, the pancreas (Fig. 3), which was largely overlapping with and blocked by the spleen and kidney and was not clearly distinguishable from the video-rate imaging alone. This demonstrates the unique ability of PCA to extract individual organ information from seemingly nonspecific signal during imaging.

Because PCA is sensitive to large fluctuations, it is important to confirm that features observed are not artifacts created by breathing motions of the animal. To confirm that the breathing motions did not have an effect on the data, PCA was also run on a dataset where breathing frames were manually removed (see Movie S3). Removal of breathing frames was equivalent to removing approximately 1 out of every 3 s of the original video. The results of PCA run on the edited dataset (Fig. S4) showed similar anatomical resolution, as shown in Fig. 3. In particular, this indicates that the pancreas signal observed is not an effect of splenic movement during breathing.

Time-Dependent PCA. Although PCA is a terrific tool for converting time correlation into spatial resolution, it comes at the cost of sacrificing temporal information. To get anatomical information from a time series of images, the images are compressed into orthogonal components. The insight of spatial resolution of features comes at the cost of temporal resolution. In an attempt to achieve both spatial and temporal resolution, we applied PCA over an expanding window over the time series. In this way, the features from the early time points (lung, kidney) are maintained, and features that appear later (liver, spleen, pancreas) change in appearance over different windows. This time-dependent PCA

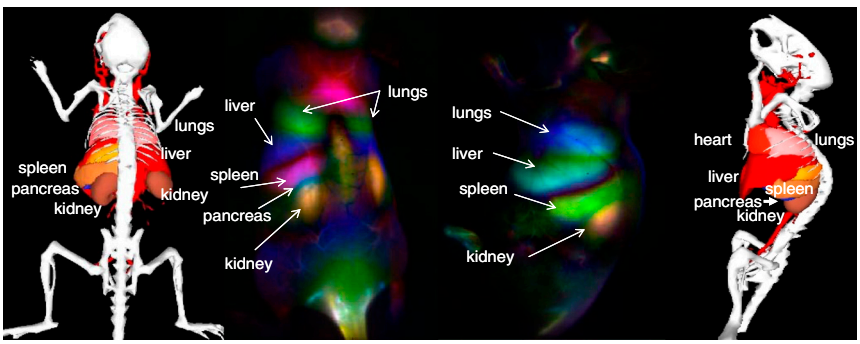

Fig. 3. Dynamic contrast-enhanced imaging with SWNTs through PCA. PCA images taken over the first 130 s following injection performed by taking every 150 evenly spaced frames out of the 2,000-frame dataset. Major features observed belong to the lungs, liver, kidney, and spleen. Of note is the appearance of the pancreas in the interstitial space between the kidney and spleen (see text for details). This feature is not observable in the raw time-course images.

analysis was done to observe the prominence and clarity of individual organs over time (Fig. 4 and Fig. S5). In agreement with the ROI time-course data (Fig. 2 *I* and *J*), the lung and kidneys are the prominent features when PCA is done over the initial time periods, as shown in the negative and combined PCA time-course images taken over the first 30 s p.i. (Fig. 4 *B* and *C* and Fig. S5). Over the first 50 s p.i.. (Fig. 4 *A* and *C* and Fig. S5), the positive and combined PCA time-course images show increasing liver and spleen clarity as a function of time. It should be noted that the appearance of an organ in the time-course PCA images is an indication of high variance of those pixels in time. The appearance of the organ does not necessarily indicate uptake, nor the direction of the variance in time, be it increasing in intensity or decreasing.

One of the powers of PCA applied in this way is the ability to resolve features that cannot be seen from the raw images. The negative PCA time-course images show the blue pancreas feature becoming increasingly apparent over time (Fig. 4*B* and Fig. S5). The feature first appears at 80 s p.i. and grows in size and clarity until 130 s p.i.. This contrasts with the positive PCA time-course images, which contain information about the RES organs (liver, spleen) that show different temporal behavior than the pancreas (Fig. 4*A* and Fig. S5). The liver and spleen show up clearly at 50 s p.i. and increase in clarity with time. This difference in temporal behavior is a key piece of evidence that the pancreas and spleen features are in fact distinct. This temporal difference is further elucidated by an ROI time course taken over the positive pixels of the second principle component (spleen) and the negative pixels of the fourth principle component (pancreas) (Fig. S6).

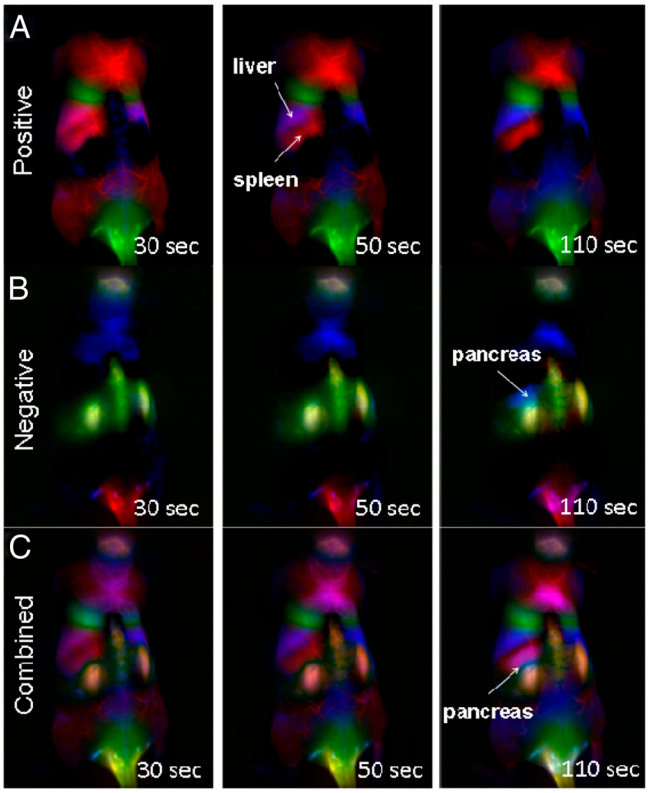

Fig. 4. Time-dependent PCA images of mouse anatomy with SWNTs. (*A*) Positive pixels of time-dependent PCA, showing the liver and spleen of the RES. The liver and spleen show increasing clarity as a function of time. (*B*) Negative pixels from time-dependent PCA showing kidney features at 30, 50, and 110 s. The pancreas appears as a blue spot above the left kidney in the 110-s image. (*C*) Absolute value of pixels from time-dependent PCA analysis, showing increased clarity of liver and spleen as a function of time and a distinct blue pancreas feature at 110 s.

Further, the combined PCA images show that the pancreas and spleen features are spatially distinct. Careful inspection of the combined PCA time-course images at 50 and 110 s p.i.. (Fig. 4*C* and Fig. S5) shows the appearance of a blue spot between the spleen and kidney features. The spatial difference, combined with the temporal evidence discussed above, indicates that these two features are in fact distinct. The identification of this distinct feature was done by examining the mouse anatomy using Living Image software (Fig. S7). The only organ between the spleen and kidney is in fact the pancreas. The fact that the pancreas can be resolved beneath the spleen and kidney shows the depth penetration of the NIR II–emitting SWNT probe and the power of time-dependent PCA to resolve buried features.

Depth Penetration: NIR I Versus NIR II. The dynamic contrast images shown here provide evidence that SWNTs can be a useful tool for fast and sensitive fluorescent imaging. The contention of Hillman and Moore (19) was that the use of an NIR I dye (ICG) was beneficial because of the deeper tissue penetration and lower autofluorescence in this region. We propose the NIR II–emitting dyes may be even more useful for this type of imaging, because of further reduction of autofluorescence (which is mostly confined to the visible) (26–32) and deeper tissue penetration. We further propose that the far red emission of SWNTs minimizes scattering, which is the main culprit in the loss of image fidelity and integrity. Whereas tissue absorption can be compensated for with higher excitation power and/or a brighter probe, scattering of light leads to loss of image information and is difficult to compensate or correct by any means.

Mock tissue phantom depth penetration studies were performed to investigate the effect of an absorbing and scattering medium (Intralipid®) on emitters in the NIR I (ICG) and

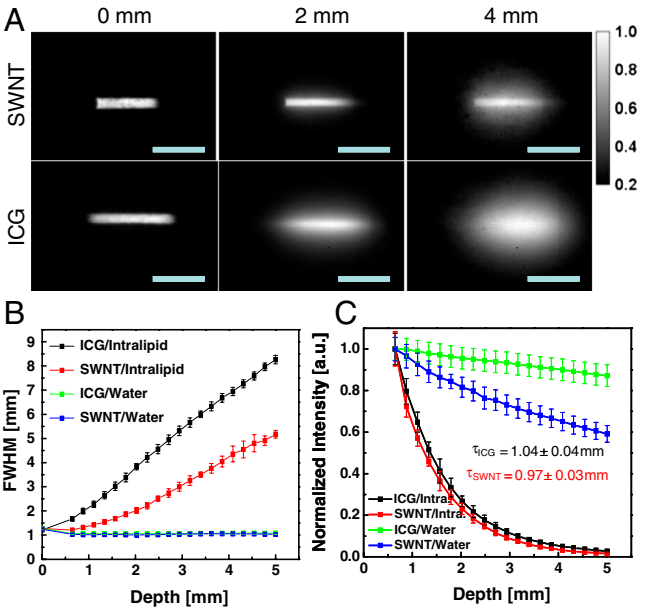

Fig. 5. Tissue phantom study of the depth penetration of SWNTs and ICG. (*A*) Fluorescence images of capillaries of SWNTs (NIR II) and ICG (NIR I) at depths of 0, 3, and 5 mm in Intralipid® excited at 785 nm. The SWNT sample shows less feature spread than that of the ICG sample. Scale bars represent 1.5 cm. (*B*) Feature width of SWNT and ICG capillary images as a function of depth in Intralipid®, showing increased loss of feature integrity for the NIR I–emitting ICG compared to the NIR II–emitting SWNT. Control experiments performed in water show no change in feature size for both ICG and SWNT. Error bars are derived from the uncertainty in the fitting of feature width. (*C*) Intensity decay of ICG and SWNT as a function of depth in Intralipid® and water. Despite the greater absorption of water in NIR II, the decay of signal in the Intralipid® phantom is similar for both ICG and SWNT, showing exponential decay depths of 1.04 ± 0.04 and 0.97 ± 0.03 mm respectively.

NIR II (SWNT) (Fig. 5). With increased depth, there is a qualitative and quantitative loss of image clarity and broadening of feature width. This is a direct result of the increased scattering as function of wavelength, which for Intralipid® is governed (33) by $\sim\lambda^{-2.4}$. Experimental studies have shown that most tissue follows the scattering behavior to varying degrees, with skin showing very high wavelength dependence (Fig. 1*D*) (8, 9). Intralipid® is known to have similar scattering properties and was chosen for this reason (9).

The measured intensity profiles versus depth for NIR I and NIR II fluorophores were quite similar (Fig. 5*c*). This indicates that the depth penetration, as defined as a combination of both absorption and scattering, and measured as the surviving intensity of light, is similar in both cases (4). Fitting an exponential function to these curves gives a characteristic depth penetration of 1.04 ± 0.04 and 0.97 ± 0.03 mm for ICG and SWNT respectively. The close similarity is due to the fact that for the NIR II emitter, the increased absorbance in water relative to the NIR I emitter, is compensated by a decreased scattering probability. This scattering effect is evidenced by the fact that the spread in the image increases significantly as a function of tissue depth and is more pronounced in the NIR I region than in the NIR II region (Fig. 5 *A* and *B*). Because of the inverse wavelength dependence of scattering ($\sim\lambda^{-2.4}$ for Intralipid®), the NIR I region is characterized by higher albedo (i.e., high percentage of extinction due to scattering), and the loss of signal is correlated with a loss of feature contrast. The loss of image information is a direct result of a higher frequency of scattering events encountered by photons as they travel through turbid media. The scattering changes both the position and direction with which light leaves the medium relative to its starting trajectory, leading to a larger spread in the image features and confusion of feature information. The NIR II is a region of lower albedo, where the extinction is mainly dominated by absorption of water. In this region, the frequency of scattering events is lower, leading to better maintenance of feature information. Control experiments performed in a nonscattering medium (water; Fig. 5*B*) show no spread of feature width with increasing depth. The loss of image integrity at shorter wavelengths is also observed in Monte Carlo simulations on a point source emitter (Figs. S8 and S9), using water and Intralipid® as the major factors for absorption and scattering, respectively. Despite the simple nature of the simulation, representing a single point rather than a macroscopic object, the qualitative trend is the same, with the NIR I showing greater loss of feature integrity with increasing depth. It should be noted that the extinction by an absorption event can be compensated for, especially in situations where the signal to background ratio is high (i.e., low autofluorescence, as in the NIR II), whereas a scattering event leads to confusion of the initial feature information including broadened feature sizes.

SWNTs show promise as an NIR II emitter for imaging in the low albedo domain. The NIR II region is not only characterized by low scattering, but also by low autofluorescence (26). This benefit is further enhanced by a large Stokes shift between emission and excitation resonances [≥300 nm; see Fig. S10 for photoluminescence excitation/emission (PLE) spectrum], leading to further suppression of endogenous autofluorescence (18, 34). One issue is that the relatively low quantum yield (QY) of SWNTs may limit its future applications. Recent studies using separation and surface modification have led to somewhat enhanced QY (35, 36), but further work needs to be done to apply these nanotubes to biological imaging. The development of new, brighter emitters such as semiconductor QDs and organic fluorophores in the NIR II will make exploitation of this advantageous region even more fruitful.

Conclusion

We have shown that SWNTs are useful fluorophores in the low albedo NIR II region. These fluorophores are bright enough to be imaged deep inside mice at high frame rate without excessive excitation power. Dynamic information from the raw images and ROI time courses, along with time-dependent PCA analysis, indicated that the circulation pathway of tail-vein–injected SWNTs is from lungs to kidneys, followed by circulation in organs belonging to the RES system, represented in this work by the liver and spleen. PCA was also able to resolve the pancreas, which is buried beneath the spleen and kidney and was not observable in the raw time-course images.

We have also shown that the NIR II emission window shows inherent advantages over the more commonly used NIR I window. Because of the lower albedo in this range, image contrast and feature sizes are better preserved with increased tissue thickness while low endogenous autofluorescence allows for easy discrimination between signal and background. This low background also allows for increased excitation power to compensate for absorption of water and further increase the advantage of the NIR II window.

Because of the low background and low scattering, high anatomical resolution is possible in the NIR II region using PCA-based dynamic contrast imaging. This dynamic contrast imaging may allow for many future applications, including the identification of tumors due to the differential blood flow rate of leaky tumor vessels. Furthermore, PCA imaging with high spatial resolution may be able to diagnose diseases that affect the size and shape of organs without the need for radioactive tags or MRI.

Methods

Complete methods can be found in *SI Text*.

Preparation of Biocompatible SWNT Fluorophores with High Relative QY. The preparation of brightly fluorescent exchanged-SWNTs with high biocompatibility can be found in detail in ref. 18 by using a surfactant exchange method to minimize damage to SWNTs. A fluorescence emission spectrum of the resulting SWNTs with DSPE-mPEG coating at 808-nm excitation is shown in Fig. 1*B*. A PLE spectrum of the DSPE-mPEG SWNTs can be found in Fig. S10.

Video-Rate NIR II Imaging. Video-rate imaging was performed on a homebuilt setup consisting of a 2D InGaAs array (Princeton Instruments). The geometry of the imaging setup is shown in Fig. 1*A*. The excitation light was provided by a fiber-coupled 808-nm diode laser (RMPC Lasers), chosen to overlap with the traditional biological transparency window. The light was collimated by a 4.5-mm focal length collimator (ThorLabs) and filtered to remove unwanted radiation in the emission range. The excitation spot was a circle with a diameter of approximately 6 cm. The excitation power at the imaging plane was approximately 5 W, leading to power density of approximately 140 mW/cm^2. Emitted light was passed through a 1,100-nm longpass filter (ThorLabs FEL1100) and focused onto the detector by a lens pair consisting of two NIR achromats (200 and 75 mm; Thorlabs). The 1,100-nm longpass filter was chosen to select the majority of the wavelength emission, while rejecting autofluorescence that may occur near the excitation band. The camera was set to expose continuously and images were acquired with LabVIEW software at highest possible frame rate. The exposure time for all images shown is 50 ms. There was a 19-ms overhead in the readout, leading to an average time of 69 ms between consecutive frames. Two thousand consecutive frames were collected, leading to a total imaging time of 2 min and 18 s. For imaging, five female athymic nude mice were used, and results shown are representative. The ideal concentration for injection and video-rate imaging was determined to be 200 μL of approximately 500-nM SWNT solution (optical density ~4 at 808 nm) (37).

Mouse Handling and Injection. Female athymic nude mice were obtained from Harlan Sprague Dawley. All experiments were in accordance with Institutional Animal Care and Use Committee protocols. For SWNT injection, a 30-gauge catheter was inserted into the lateral tail vein, allowing for bolus injection during the first frames of imaging.

Dynamic Contrast-Enhanced Images. Dynamic contrast-enhanced images were obtained in a similar fashion to the seminal work by Hillman and Moore (19).

All 2,000 video frames were loaded into an array using MATLAB software, and the princomp function was used to perform PCA. PCA was performed using 150 frames evenly spaced over the entire dataset. For "positive" images, the positive pixels for second, third, and fourth principal components were assigned red, green, and blue, respectively, and overlaid. For "negative" images, the negative pixels for second, third, and fourth principal components were assigned red, green, and blue, respectively, and overlaid. For "combined" images, the absolute value of the principal component scores were used. The construction of PCA images is shown in Fig. S3. Time-based dynamic contrast images were obtained by performing PCA over different periods of time. To conserve computing power, each time period was broken into 150 frames. For example, the 10-s dynamic contrast images were taken by performing PCA on the first 150 frames of the video. For the 30-s dynamic contrast images, PCA was performed over the first 450 frames, selecting every third frame.

Tissue Phantom Depth Penetration Study. Intralipid® was chosen as a mock tissue because of its similar scattering properties (9, 10, 33, 38). A stock of 20% Intralipid® was diluted to make a 1% solution. Glass capillary tubes were filled with either SWNT or ICG solutions to act as mock fluorescent features. The bottom portion of capillary tubes was wrapped in black tape, leaving only a small portion on the top available for imaging. The capillaries were placed in a cylindrical dish and covered with different volumes of 1% Intralipid®. The depth of the capillary was calculated from the known area of the dish. Taping of the capillary tube improved depth measurements, as the depth was calculated from the exposed, fairly level portion of the capillary tube. Excitation was provided by a 785-nm diode laser (Renishaw) coupled to a 900-μm core optical fiber. Emitted light was filtered through an 850-nm longpass filter (Thorlabs FEL850) and imaged on the 2D InGaAs array described above. To obtain depth penetration information, average intensity was taken from the same ROI at various depths and plotted as a relative intensity for each probe. Plots of relative intensity for each probe prevent differences in probe QYs and extinction coefficients from affecting the comparison. To determine feature width, linear cross-sections were taken from the images and fit to Gaussians using Origin's built-in curve fitting. Linear cross-sections taken from images, shown in Fig. S11, confirm that signal spreading is not due to phantom geometry or wavelength-dependent light interaction with the surface of the dish.

ACKNOWLEDGMENTS. This work is supported by National Institutes of Health–National Cancer Institute Grant 5R01CA135109-02 and the Stanford University Center for Cancer Nanotechnology Excellence Focused on Therapy Response.

1. Lakowicz JR (2006) *Principles of Fluorescence Spectroscopy* (Springer, New York).
2. Rust MJ, Bates M, Zhuang X (2006) Sub-diffraction-limit imaging by stochastic optical reconstruction microscopy (STORM). *Nat Methods* 3:793–795.
3. Betzig E, et al. (2006) Imaging intracellular fluorescent proteins at nanometer resolution. *Science* 313:1642–1645.
4. Splinter R, Hooper BA (2007) *An Introduction to Biomedical Optics* (Taylor & Francis, New York).
5. Britton C (1998) Near-infrared images using continuous, phase-modulated, and pulsed light with quantitation of blood and blood oxygenation. *Ann N Y Acad Sci* 838:29–45.
6. Escobedo JO, Rusin O, Lim S, Strongin RM NIR dyes for bioimaging applications. *Curr Opin Chem Biol* 14:64–70.
7. Michalet X, et al. (2005) Quantum dots for live cells, in vivo imaging, and diagnostics. *Science* 307:538–544.
8. Bashkatov AN, et al. (2005) Optical properties of human skin, subcutaneous and mucous tissues in the wavelength range from 400 to 2000 nm. *J Phys D Appl Phys* 38:2543.
9. Tamara LT, Suresh NT (2001) Optical properties of human skin in the near infrared wavelength range of 1000 to 2200 nm. *J Biomed Opt* 6:167–176.
10. Lim YT, et al. (2003) Selection of quantum dot wavelengths for biomedical assays and imaging. *Mol Imaging* 2:50–64.
11. Peng XG (2009) An essay on synthetic chemistry of colloidal nanocrystals. *Nano Res* 2:425–447.
12. Wehrenberg BL, Wang C, Guyot-Sionnest P (2002) Interband and intraband optical studies of PbSe colloidal quantum dots. *J Phys Chem B* 106:10634–10640.
13. Bakueva L, et al. (2004) PbS quantum dots with stable efficient luminescence in the near-IR spectral range. *Adv Mater* 16:926–929.
14. Harrison MT, et al. (2000) Wet chemical synthesis and spectroscopic study of CdHgTe nanocrystals with strong near-infrared luminescence. *Mater Sci Eng B Solid State Mater Adv Technol* 69–70:355–360.
15. Cherukuri P, Bachilo SM, Litovsky SH, Weisman RB (2004) Near-infrared fluorescence microscopy of single-walled carbon nanotubes in phagocytic cells. *J Am Chem Soc* 126:15638–15639.
16. Jin H, Heller DA, Strano MS (2008) Single-particle tracking of endocytosis and exocytosis of single-walled carbon nanotubes in NIH-3T3 cells. *Nano Lett* 8:1577–1585.
17. Welsher K, Liu Z, Daranciang D, Dai H (2008) Selective probing and imaging of cells with single walled carbon nanotubes as near-infrared fluorescent molecules. *Nano Lett* 8:586–590.
18. Welsher K, et al. (2009) A route to brightly fluorescent carbon nanotubes for near-infrared imaging in mice. *Nat Nanotechnol* 4:773–780.
19. Hillman EMC, Moore A (2007) All-optical anatomical co-registration for molecular imaging of small animals using dynamic contrast. *Nat Photonics* 1:526–530.
20. Liu Z, et al. (2008) Circulation and long-term fate of functionalized, biocompatible single-walled carbon nanotubes in mice probed by Raman spectroscopy. *Proc Natl Acad Sci USA* 105:1410–1415.
21. Hummel KP, Richardson FL, Fekete E (1966) Anatomy. *Biology of the Laboratory Mouse*, ed EL Green (Dover, New York).
22. Debbage PL, et al. (1998) Lectin intravital perfusion studies in tumor-bearing mice: Micrometer-resolution, wide-area mapping of microvascular labeling, distinguishing efficiently and inefficiently perfused microregions in the tumor. *J Histochem Cytochem* 46:627–639.
23. Schmidt EE, MacDonald IC, Groom AC (1985) Microcirculation in mouse spleen (non-sinusal) studied by means of corrosion casts. *J Morphol* 186:17–29.
24. Lay DC (2003) *Linear Algebra and Its Applications* (Addison–Wesley, Boston).
25. Davies B, Morris T (1993) Physiological parameters in laboratory animals and humans. *Pharm Res* 10:1093–1095.
26. Aubin JE (1979) Autofluorescence of viable cultured mammalian cells. *J Histochem Cytochem* 27:36–43.
27. Demchenko AP (1986) *UV Spectroscopy of Proteins* (Springer–Verlag, Berlin).
28. Longworth JW (1971) *Excited States of Proteins and Nucleic Acids*, eds RF Steiner and I Weinryb (Plenum, New York), pp 319–484.
29. Permyakov EA (1993) *Luminescent Spectroscopy of Proteins* (CRC, Boca Raton).
30. Gafni A, Brand L (1976) Fluorescence decay studies of reduced nicotinamide adenine-dinucleotide in solution and bound to liver alcohol-dehydrogenase. *Biochemistry* 15:3165–3171.
31. Sun M, Moore TA, Song P-S (1972) Molecular luminescence studies of flavines. I. The excited states of flavines. *J Am Chem Soc* 94:1730–1740.
32. Benjamin E, Zvi M, Yeshayahu N (1985) Fluorescence spectral changes of the hematoporphyrin derivative upon binding to lipid vesicles, *Staphylococcus Aureus* and *Escherichia Coli* cells. *Photochem Photobiol* 41:429–435.
33. Vanstaveren HJ, et al. (1991) Light-scattering in intralipid-10% in the wavelength range of 400–1100 nm. *Appl Opt* 30:4507–4514.
34. Bachilo SM, et al. (2002) Structure-assigned optical spectra of single-walled carbon nanotubes. *Science* 298:2361–2366.
35. Crochet J, Clemens M, Hertel T (2007) Quantum yield heterogeneities of aqueous single-wall carbon nanotube suspensions. *J Am Chem Soc* 129:8058–8059.
36. Ju S-Y, Kopcha WP, Papadimitrakopoulos F (2009) Brightly fluorescent single-walled carbon nanotubes via an oxygen-excluding surfactant organization. *Science* 323:1319–1323.
37. Kam NWS, O'Connell M, Wisdom JA, Dai H (2005) Carbon nanotubes as multifunctional biological transporters and near-infrared agents for selective cancer cell destruction. *Proc Natl Acad Sci USA* 102:11600–11605.
38. Stephen TF, et al. (1992) Optical properties of intralipid: A phantom medium for light propagation studies. *Lasers Surg Med* 12:510–519.